SCIENTIFIC REPORTS

OPEN

SUBJECT AREAS:
MULTIPHOTON MICROSCOPY
IMAGING AND SENSING

Received
25 February 2014

Accepted
14 May 2014

Published
5 June 2014

Correspondence and requests for materials should be addressed to V.R.S. (vrsingh@smart.mit.edu) or P.T.C.S. (ptso@mit.edu)

* These authors contributed equally to this work.

Reassignment of Scattered Emission Photons in Multifocal Multiphoton Microscopy

Jae Won Cha[1]*, Vijay Raj Singh[2]*, Ki Hean Kim[3], Jaichandar Subramanian[4], Qiwen Peng[5,6], Hanry Yu[2,5,7], Elly Nedivi[4,8] & Peter T. C. So[1,2,9]

[1]Massachusetts Institute of Technology, Department of Mechanical Engineering, Cambridge, MA 02139, [2]Singapore-MIT Alliance for Research and Technology (SMART), BioSyM, Singapore 138602, [3]Pohang University of Science and Technology, Department of Mechanical Engineering, Pohang 790-784, KOREA, [4]Massachusetts Institute of Technology, Picower Institute for Learning and Memory, Cambridge, MA 02139, [5]Institute of Bioengineering and Nanotechnology, A*Star, Singapore 138669, [6]Singapore-MIT Alliance, Computation and System Biology, Singapore 117576, [7]National University of Singapore, School of Medicine, Singapore 119077, [8]Massachusetts Institute of Technology, Departments of Biology, and Brain and Cognitive Sciences, Cambridge, MA 02139, [9]Massachusetts Institute of Technology, Department of Biomedical Engineering, Cambridge, MA 02139.

Multifocal multiphoton microscopy (MMM) achieves fast imaging by simultaneously scanning multiple foci across different regions of specimen. The use of imaging detectors in MMM, such as CCD or CMOS, results in degradation of image signal-to-noise-ratio (SNR) due to the scattering of emitted photons. SNR can be partly recovered using multianode photomultiplier tubes (MAPMT). In this design, however, emission photons scattered to neighbor anodes are encoded by the foci scan location resulting in ghost images. The crosstalk between different anodes is currently measured a priori, which is cumbersome as it depends specimen properties. Here, we present the photon reassignment method for MMM, established based on the maximum likelihood (ML) estimation, for quantification of crosstalk between the anodes of MAPMT without a priori measurement. The method provides the reassignment of the photons generated by the ghost images to the original spatial location thus increases the SNR of the final reconstructed image.

Multiphoton excitation fluorescence microscopy has inherent 3D resolution due to the nonlinear dependence of excitation upon the incident light distribution[1,2]. The excitation region is localized to a femtoliter volume at the focal point of a high numerical aperture objective lens. Multiphoton excitation fluorescence microscopy is routinely used in a variety of tissue imaging applications due to its excellent imaging depth, high resolution, and lower photo-damage. However, one of the practical limitations of multiphoton excitation fluorescence microscopy is its imaging speed, typically up to a few frames per second. While this imaging speed is sufficient in many cases, several types of applications require faster systems. These applications include the measurement of dynamic processes including calcium signaling and action potential propagation[3], high throughput image cytometric studies of tissue physiology[4,5], and clinical applications where the effects of physiological motion should be minimized. In vivo imaging of small structures, such as neuronal synapses, across a full neuronal arbor can also be problematic due to the lengthy anesthesia required to scan large volumes at high resolution[6].

High-speed multiphoton imaging has been previously implemented using several approaches. The first approach is based on using high-speed scanners such as polygonal mirrors[7], resonant mirror scanners[8], or acousto-optical deflectors (AODs)[9–12] instead of galvanometric mirror scanners used in conventional multiphoton microscopes. The high speed scanners can typically achieve a scanning speed of up to about 30 frames per second with a comparable imaging depth in tissues as conventional multiphoton microscopy. However, these high speed scanning systems require shorter pixel dwell time resulting in lower image contrast and poorer SNR. This can be partially compensated by increasing the excitation laser power, but it is not always possible due to photo-damage of the specimen and excitation saturation[13,14].

The second method is two-photon wide-field imaging[15,16]. With the temporal focusing method, a 3D resolved plane is generated at once by two-photon excitation instead of a focus eliminating the need for lateral scanner resulting in faster imaging speed. However, its performance is often limited by the lower axial resolution compared with conventional multiphoton microscopy and lower SNR due to the scattering of emission photons.

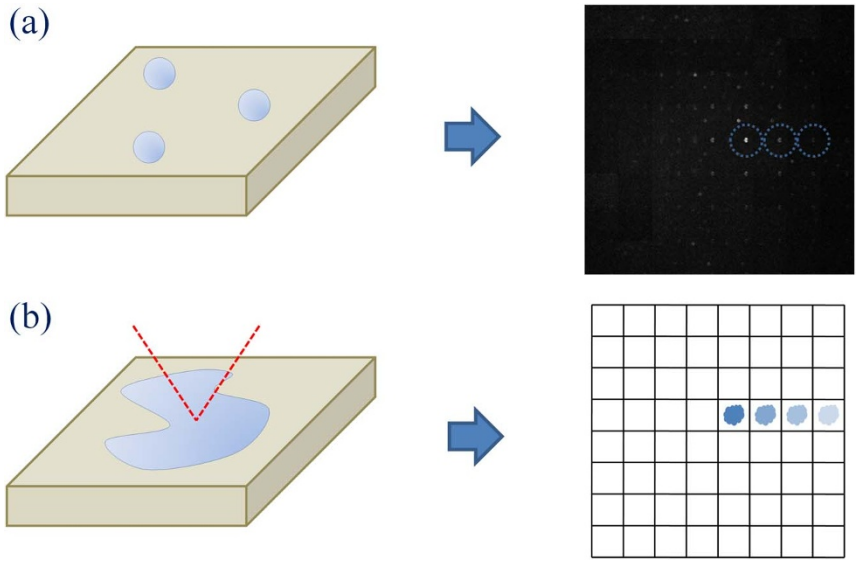

Figure 1 | Two experimental approaches for the estimation of a scattering matrix. (a) Sparsely distributed beads sample in tissue phantom (2% Intralipid emulsion), and scattering matrix measurement from its MMM image. (b) Single focus excitation on a real sample and scattering matrix measurement from its MMM image.

The third method is multifocal multiphoton microscopy (MMM), which is an intermediate approach between the two previously described techniques[17–22]. With a lenslet array or diffractive optical element (DOE)[23,24], a number of foci are generated simultaneously and scanned together. The size of the whole scanning region corresponds to the sum of the sub-region scanned by each focus. Therefore, the imaging speed is improved proportionally to the number of foci. One practical limitation for the imaging speed of MMM is available laser power. For typical titanium-sapphire laser with several Watts of output, approximately one hundred foci can be effectively generated for tissue imaging resulting in approximately two orders of magnitude improvement in imaging speed.

Similar to two-photon wide-field imaging, the SNR of multifocal multiphoton microscopy is also limited by the tissue scattering of emission photons resulting in lower SNR compared with single focus scanning multiphoton microscopy. Simultaneous detection of multiple foci requires detectors with spatial resolution that can distinguish signals from all the foci at the same time. Most multifocal multiphoton microscopes use imaging detectors such as CCD or CMOS cameras. However, when emission photons generated at one focus are scattered in a turbid specimen and arrive at detector pixels that do not map to the focus location, the SNR of the image suffers. This lower SNR can be compensated by the use of multianode photomultiplier tubes (MAPMT) in a descanned detection geometry[25]. The larger detection area of each anode greatly reduces the crosstalk between foci due to the scattering of emission photons and significantly improves the image SNR.

However, with severe scattering in a turbid specimen, especially at larger imaging depth, scattered emission photons will still arrive at neighboring anodes, resulting in the formation of ghost images, which are duplicates of the image acquired by one focus visualized in neighbor sub-images. To remove the ghost images and to increase the SNR of the original image, these scattered emission photons should be reassigned to their original pixels. We have shown that this can be accomplished by estimating the scattering matrix at one location of the specimen that characterizes the crosstalk between the anodes of the MAPMT due to emission photon scattering. By applying the inverse of the scattering matrix to the acquired image, an improved SNR picture free from ghost images can be produced. The estimation of the scattering matrix was done experimentally[25] (Fig. 1). The first method of the estimation is using a tissue phantom with similar optical parameter as real tissues containing sparsely distributed fluorescence particles. These fluorescence particles are imaged by the MMM. The sparsity of the particles ensures that the ghost images of each particle can be identified. By measuring the relationship between particle intensities in the correct pixel and all its neighbors, the scattering matrix can be calculated. However, the phantom sample is often a poor model of a real tissue specimen on the microscopic level where there is significant heterogeneity, potentially leading to a significant error in image post-processing. Second, the scattering matrix can be calculated with a real sample by exciting only one focus at a time in the same MMM system. This method gives the exact coefficients for the scattering matrix. However, since the scattering matrix is a function of specimen location, due to heterogeneity, and depth, due to increased scattering, scattering matrix must be measured frequently. This labor intensive measurement process partly negates the speed advantage of applying MMM imaging.

In this work, we demonstrate a novel image post-processing approach for MMM that allows estimation of the scattering matrix without any additional experimental measurement. The proposed approach is based on maximum likelihood estimation quantifying the crosstalk between the different anodes of the MAPMT based on the actual optical model of the MMM system. This approach reassigns the photons that are originally detected at wrong anodes, appearing as ghost images, to the correct anode location. Therefore, it greatly improves signal strength and simultaneously minimizes ghost images in the neighboring sub-images. Since the proposed approach uses only the images generated by the MMM without any tissue dependent a priori information, the characterization of the scattering matrix can be estimated at each location and depth. A mathematical model of the proposed approach is presented and validated first with simulation data where the results show the convergence of the method to the actual fluorophores structures. The performance of the proposed method is then employed for fluorescence beads and mouse neuron images where the results are quantitatively analyzed.

Methods

MMM configuration. We have developed two MMM systems; one with 45 μm foci separation, and the other with 85 μm foci separation. Fig 2 shows the schematic of the MMM with 85 μm foci separation based on a diffractive optical element (DOE) for multiple foci generation and the MAPMT in descanned detection geometry. The light source used is Chameleon Ultra II (Coherent, Santa Clara, CA). The excitation laser beam is expanded and illuminates the 8 × 8 or 4 × 4 DOE (customized, Holo/Or, Rehovoth, Israel) depending on the excitation wavelengths (8 × 8 for 780 nm and 4 ×

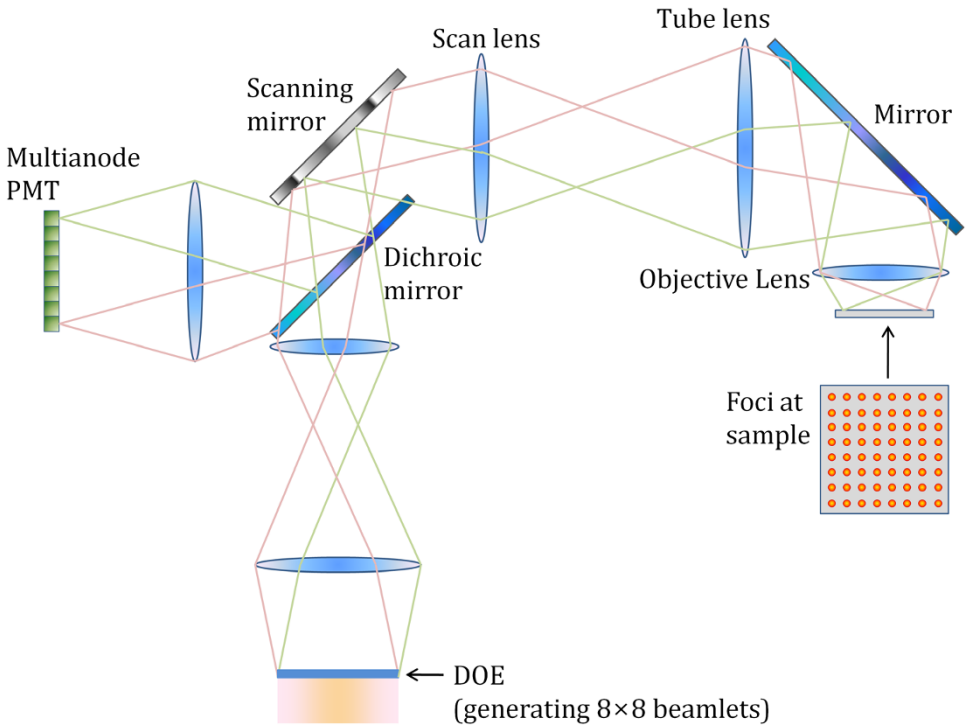

Figure 2 | Schematic of MMM based on the MAPMT.

4 for 910 nm). The beamlets are shrunk according to the size of x-y galvanometric mirror scanners (6215H, Cambridge Technology, Lexington, MA), and are overlapped on the scanning mirrors. The beamlets reflected by the scanners are expanded again to fill the back focal plane of a 20× water immersion objective lens with 1.0 NA (W Plan-Apochromat, Zeiss, Thornwood, NY), and enter the aperture with different entrance angles. The objective lens generates an array of 8 × 8 or 4 × 4 excitation foci on the focal plane in a specimen. The image is formed by raster scanning of the excitation foci across the specimen using the scanning mirrors. The excitation foci are separated from each other by 85 μm, and each focus scans slightly larger than the area of 85 μm × 85 μm in the sample plane to facilitate the montage assembly. The scan area covered by the 8 × 8 foci is 680 μm × 680 μm with the 85 μm separation, and 340 μm × 340 μm by the 4 × 4 foci. The emission photons are collected by the same objective lens and descanned by the scanning mirrors. The descanned emission beamlets are essentially stationary in relation to the scanning speed. The emission beamlets are reflected by a dichroic mirror (Chroma Technology, Bellows Falls, VT) toward the MAPMT and are focused onto the center of each corresponding anode of the MAPMT (H7546B-20, Hamamatsu, Bridgewater, NJ). An IR blocking filter (BG39, Chroma Technology, Bellows Falls, VT) and a short-pass filter (ET680sp-2p, Chroma Technology, Bellows Falls, VT) is installed before the MAPMT to block the excitation light. The MMM system with 45 μm foci separation has a very similar system configuration, but uses a different model Ti-Sapphire (Ti-Sa) laser (Tsunami, Spectra-Physics, Mountain View, CA) pumped by a continuous wave Nd:YVO_4 laser (Millennia, Spectra-Physics, Mountain View, CA) as a light source, a different 8 × 8 micro-lenslet array (1000-17-S-A, Adaptive Optics, Cambridge, MA), and a different 0.95 NA objective lens (XLUMPLFL20XW, Olympus, Melville, NY). In this case, the 8 × 8 foci with 45 μm foci separation cover a 360 μm × 360 μm scan area in the specimen.

Image reconstruction methodology. Let $O(x,y,z)$ be the fluorophores distribution in the specimen assuming constant irradiance per unit volume with the specimen. For two-photon point excitation at scan position $\vec{x}'$, the excitation intensity distribution at the specimen projected by an objective with a normalized 3D intensity PSF $h(\vec{x})$ is $E(\vec{x},\vec{x}') = E_o\delta(\vec{x}-\vec{x}')\otimes h(\vec{x}) = E_o h(\vec{x}-\vec{x}')$. Here E_0 is the maximum intensity and the symbol, $\otimes$, represents the 3D convolution operator. The fluorescence intensity generated at the specimen due to two-photon process is:

$$F(\vec{x},\vec{x}') = E_0^2 h^2(\vec{x}-\vec{x}')\cdot O(\vec{x}) \tag{1}$$

The effect of emission photon scattering can be modeled generally by a emission PSF $h_m(\vec{x})$. Assume $h_m(\vec{x}) = h(\vec{x})$ in the absence of scattering and $h'(\vec{x})$ represents the PSF for the scattered emission photon.

$$h_m(\vec{x}) = (1-\alpha)h(\vec{x}) + \alpha h'(\vec{x}) \tag{2}$$

Without the emission scattering effect, the emission photon scattering strength, α, is zero. In general[25], even in the presence of scattering, the amplitude of the modification term is generally small. Also, it has been observed that $h'(\vec{x})$ typically has full-width-at-half maximum that is orders of magnitude larger than that of $h(\vec{x})$[25].

The intensity distribution at the image plane in epi-detection geometry is:

$$I(x,y,\vec{x}') = [E_0^2 h^2(\vec{x}-\vec{x}')\cdot O(\vec{x})]\otimes h_m(\vec{x})|_{z=0} \tag{3}$$

For the MMM system, let $N \times N$ equally spaced foci be arranged on a rectilinear grid with reference positions $\{\vec{x}^0_{1,1},.....\vec{x}^0_{N,N}\}$, where $\vec{x}^0_{m,n} = \{m\Delta, n\Delta, 0\}$, m and n are the foci indices, and Δ is the separation distance between foci. In order to generate an image using MMM, this grid of foci must be scanned to cover each $\Delta \times \Delta$ sub-regions for the corresponding axial plane. The signal for an MMM system at location (x,y) of an imaging sensor (CCD or CMOS) at any scan location (i,j,k) can be written as,

$$\begin{aligned} I_{MMM}(x,y,i,j,k) &= \sum_{m,n}^{N,N} I(x,y,\vec{x}^0_{m,n}+\vec{x}'_{i,j},\vec{x}'_k) \\ &= \sum_{m,n}^{N,N} \{[E_0^2 h^2(\vec{x}-\vec{x}^0_{m,n}-\vec{x}'_{i,j})\cdot O(\vec{x}+\vec{x}'_k)]\otimes h_m(\vec{x},k)\}|_{z=0} \end{aligned} \tag{4}$$

For a given z-plane, k, using an imager (such as a CCD or CMOS camera with sensor size $M \times M$) that integrates the signal for all the lateral scan steps, the final single plane image can be written as:

$$\begin{aligned} I_{MMM}(x,y,k) &= \sum_{i,j}^{M,M} I_{MMM}(x,y,i,j,k) \\ &= \sum_{i,j}^{M,M}\sum_{m,n}^{N,N} \{[E_0^2 h^2(\vec{x}-\vec{x}^0_{m,n}-\vec{x}'_{i,j})\cdot O(\vec{x}+\vec{x}'_k)]\otimes h_m(\vec{x},k)\}|_{z=0} \end{aligned} \tag{5}$$

It is clear that in this case, the final image is "blurred" by the emission PSF and SNR is degraded. Instead of using an imager such as a CCD, we can also use a multianode PMT. By doing so there are two main differences[25]: (i) the image is descanned in the multianode PMT to ensure that the foci are center at each anode of the PMT, and (ii) the signal at each anode is integrated at each scanning step.

$$\begin{aligned} I_{MD}(x,y,i,j,k) &= \sum_{m,n}^{N,N} \{[E_0^2 h^2(\vec{x}-\vec{x}^0_{m,n}-\vec{x}_{i,j}')\cdot O(\vec{x}+\vec{x}'_k)]\otimes h_m(\vec{x},k)\}\big|_{z=0,x=x+i\Delta/M,y=y+j\Delta/M} \\ &= \sum_{m,n}^{N,N}\int dx''dy''dz'' E_0^2 h^2(x''-m\Delta-i\Delta/m, y''-n\Delta-j\Delta/M, z'') \\ &\quad \cdot O(x'',y'',z''+k\Delta')h_m(x-x'',y-y'',z-z'',k)\big|_{z=0,x=x+i\Delta/M,y=y+j\Delta/M} \\ &= \sum_{m,n}^{N,N}\int dx''dy''dz'' E_0^2 h^2(x''-m\Delta-i\Delta/M, y''-n\Delta-j\Delta/M, z'') \\ &\quad \cdot O(x'',y'',z''+k\Delta')h_m(x+i\Delta/M-x'', y+j\Delta/M-y'', -z'', k) \end{aligned} \tag{6}$$

For specimen with tissue-like scattering property, we may assume $h'(\vec{x})$ to be broad and smooth on the length scale of Δ. Therefore, the integrand of the integral may be replaced by a set of constant values $C_{(a,b),(m,n),k}$ that are related to the radially integrated PSF (H_0) of the scattered light. Here (a,b) are the anode index and (m,n) are the foci index. The elements of C matrix is depth dependent, specified by k for the given z-plane. Considering that the emission PSF can be further separated into a part taking into account of scattering, Eqn. (6) can now be rewritten as,

$$I_{MD}(a,b,i,j,k) = (1-\alpha(k))E_0^2 H_0 \int dx''dy''dz'h^2(x'',y'',z')\cdot O(x''+a\Delta+i\Delta/M, y''+b\Delta+j\Delta/M, z'+k\Delta') + \alpha(k)E_0^2 \sum_{m,n}^{N,N} C_{(a,b),(m,n),k} \int dx''dy''dz'h^2(x'',y'',z')\cdot O(x''+m\Delta+i\Delta/M, y''+n\Delta+j\Delta/M, z'+k\Delta') \quad (7)$$

Then equation (7) can be further simplified as:

$$I_{MD}(a,b,i,j,k) = (1-\alpha(k))H_0 I(a,b,i,j,k) + \alpha(k)\sum_{m,n}^{N,N} C_{(a,b),(m,n),k} I(m,n,i,j,k) \quad (8)$$

Note that we have generalized the emission photon scattering strength, $\alpha(k)$, to be depth dependent but invariant over each 2D plane. The detection process consists of measured photon count by each anode (a,b) at each scan location (i, j, k), i.e. $N(a,b,i,j,k)$. $N(a,b,i,j,k)$ should follow Poisson statistics with a mean given by $I_{MD}(a,b,i,j,k)$.

Maximum Likelihood Estimation. The log-likelihood function of the readout process, described in eqn. (8), can be written as.

$$l_S = \sum_{a,b,i,j,k} [N(a,b,i,j,k)\ln I_{MD}(a,b,i,j,k) - I_{MD}(a,b,i,j,k)] \quad (9)$$

This log-likelihood function utilizes the actual optical model of the MMM for the maximum likelihood estimation of specimen fluorophore distribution. Our approach provides maximization of log-likelihood function and, thus, provides the quantification of the scattering matrix that is used for the reassignment of the image photons originally recorded as ghost image photons by the neighboring anodes of MAPMT to the correct spatial location. Therefore, photon reassignment can be casted as a blind deconvolution problem that seeks to recover the image $I_{MD}(a,b,i,j,k)$, the depth dependent emission photon scattering strength, $\alpha(k)$, and the mixing kernel, $C_{(a,b),(m,n),k}$ given $N(a,b,i,j,k)$.

The original fluorophores distribution at the corresponding axial depth recorded by the MMM system can be considered as the 'first guess' for the iteration process and the maximization of log-likelihood function can be performed using a numerical optimization method which iteratively improves the strength of the actual signal by reassignment of ghost-image photons to the correct spatial location. We adopted Newton's method for maximizing the log-likelihood function and the iteration step for maximum likelihood estimation of fluorophores distribution can be written as:

(i) Maximization of the likelihood function with respect to $I(a,b,i,j,k)$ to get a better estimation for this variable:

$$\hat{I}^{(k+1)}(a,b,i,j,k) = \hat{I}^{(k)}(a,b,i,j,k) - \frac{\left\{\frac{\partial l_s(I,H_0,C,\alpha,k)}{\partial I(a,b,i,j,k)}\right\}_{I(a,b,i,j,k)=\hat{I}^{(k)}(a,b,i,j,k)}}{\left\{\frac{\partial^2 l_s(I,H_0,C,\alpha,k)}{\partial I^2(a,b,i,j,k)}\right\}_{I(a,b,i,j,k)=\hat{I}^{(k)}(a,b,i,j,k)}} \quad (10)$$

(ii) Maximization of likelihood function with respect to C to get a better estimation for this variable:

$$\hat{C}^{(k+1)}_{(a,b),(m,n),k} = \hat{C}^{(k)}_{(a,b),(m,n),k} - \frac{\left\{\frac{\partial l_s(I,H_0,C,\alpha,k)}{\partial C_{(a,b),(m,n),k}}\right\}_{C_{(a,b),(m,n),k}=\hat{C}^{(k)}_{(a,b),(m,n),k}}}{\left\{\frac{\partial^2 l_s(I,H_0,C,\alpha,k)}{\partial C^2_{(a,b),(m,n),k}}\right\}_{C_{(a,b),(m,n),k}=\hat{C}^{(k)}_{(a,b),(m,n),k}}} \quad (11)$$

(iii) Maximization of likelihood function with respect to α to get a better estimation for this variable:

$$\hat{\alpha}^{(k+1)} = \hat{\alpha}^{(k)} - \frac{\left\{\frac{\partial l_s(I,H_0,C,\alpha,k)}{\partial \alpha}\right\}_{\alpha=\hat{\alpha}^{(k)}}}{\left\{\frac{\partial^2 l_s(I,H_0,C,\alpha,k)}{\partial \alpha^2}\right\}_{\alpha=\hat{\alpha}^{(k)}}} \quad (12)$$

Here $\hat{I}^{(k)}$, $\hat{C}^{(k)}$, and $\hat{\alpha}^{(k)}$ are the estimated fluorophores distribution, scattering matrix coefficients, emission photon scattering strength respectively at k^{th} iteration step. The maximization process simultaneously updates the new estimate of $\hat{I}^{(k+1)}$, $\hat{C}^{(k+1)}$, and $\hat{\alpha}^{(k+1)}$ for iterative step k. The log-likelihood function is evaluated at each iteration step for maximum likelihood estimation of fluorophores distribution. The accuracy of this estimation partly depends on the initial estimates chosen and on the constrained parameters, i.e., positivity of the fluorophores. In the manuscript, we describe the process evaluating initial estimates of the unknown parameters from the recorded MMM image and show the applicability of the proposed method for simulation and experimental results. Fig. 3 provides the summary of the proposed photon reassignment algorithm for the MMM system.

Results

Simulation results. *4 Spots in a 2 by 2 MMM image.* To test the feasibility of our approach, we started from the simplest case using simulations. We simulated a replica of a 4 bead image in a 2 by 2 MMM [Fig. 4(a–(b))]. Fig. 4(a) shows the original image of 4 beads

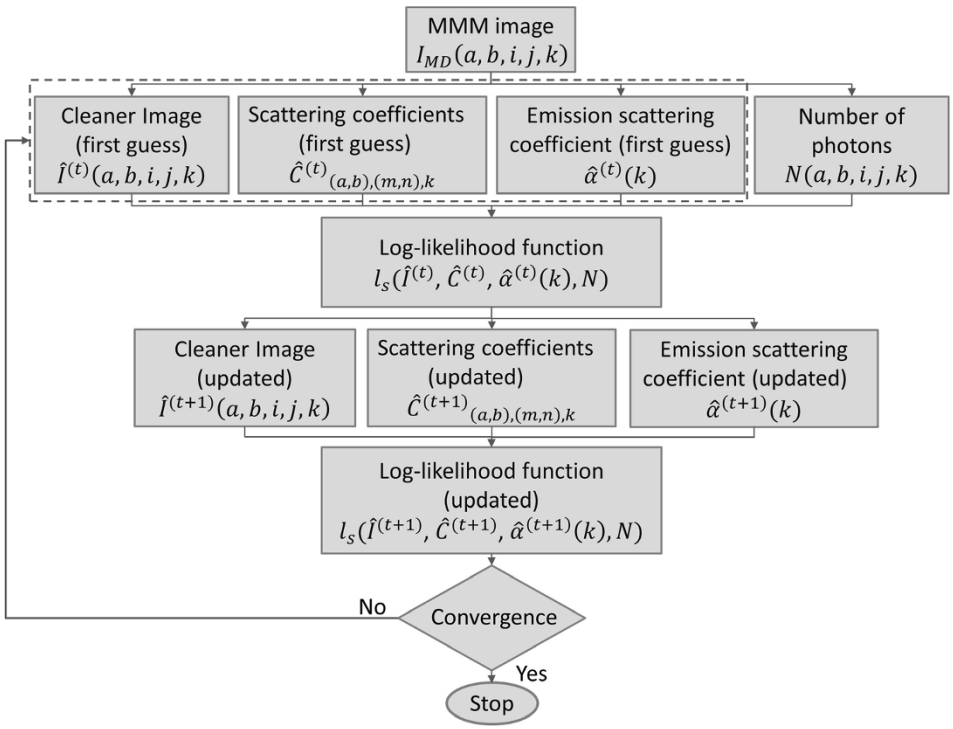

Figure 3 | Summary of the photon reassignment process for MMM.

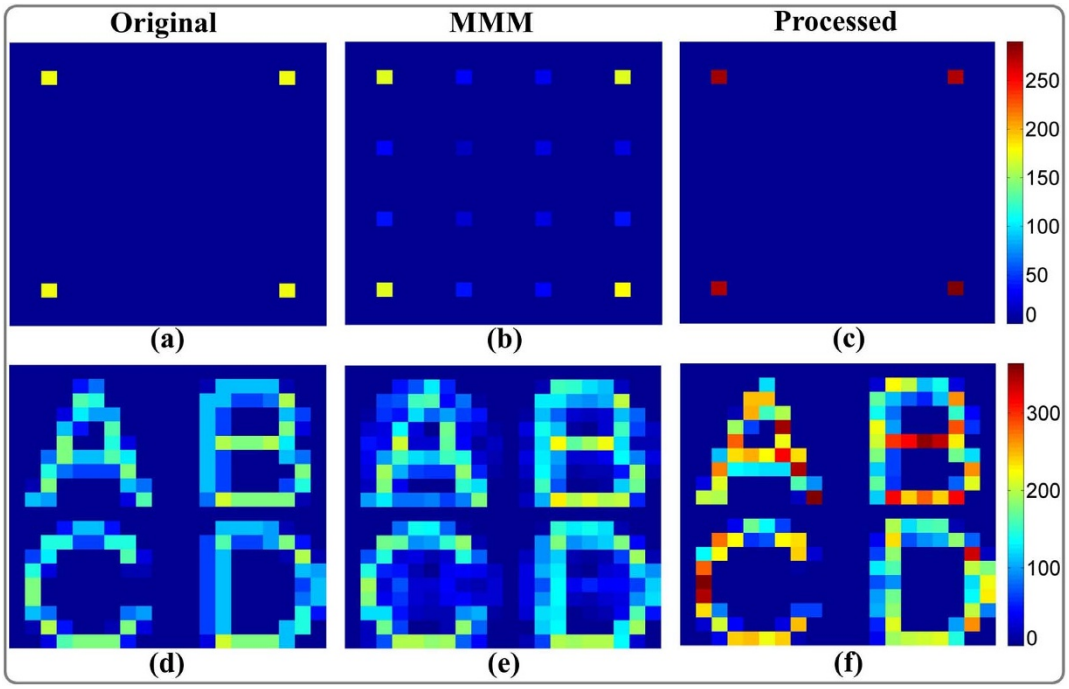

Figure 4 | (a) Original 4 beads image in a 2 by 2 MMM. (b) A scattering-affected image of (a); one sub-image contains one primary bead image and three ghost bead images with the specified proportions. (c) The processed image of (b). (d) Original alphabet image in a 2 by 2 MMM. (e) A scattering-affected image of (d) in the same fashion. (f) The processed image of (e).

without ghost images, which would be the target of our simulation. For the MMM image, shown in Fig. 4(b), each sub-image contains one primary bead image with three ghost bead images, and for the sake of simplicity there is no overlap between the beads. Any scattering-simulated sub-image contained 100% of the intensity of the primary bead, 20% of the intensity of the adjoining beads, and 14% of the intensity of the diagonal bead. We added Poisson noise in the simulated image by using the '*imnoise*' function of MATLAB (MathWorks, Natick, MA). The proposed method requires the first guess of the cleaner image $\hat{I}^{(1)}(a,b,i,j,k)$, scattering matrix coefficients $\hat{C}^{(1)}_{(a,b),(m,n),k}$, and emission photon scattering strength$\hat{\alpha}^{(1)}$. We chose the actual MMM image as the first guess for the cleaner image. In order to keep the proposed method adaptive, and to automatically generate the first guess for scattering matrix coefficients and emission photon scattering strength we used the following steps:

(i) Identify the spatial position of the pixel (and its MAPMT anode) that contains the maximum intensity in the entire MMM image.
(ii) Observe the intensities at the pixels corresponding to same spatial location of all the neighboring anodes identified in step (i).
(iii) Generate the intensity ratios of the maximum value pixel to neighboring anode pixels.
(iv) Repeat the steps (i)–(iii) for a few more values next to the maximum intensity, if possible, and take the mean of the all these values (coefficients of the scattering matrix).
(v) More coefficients of the scattering matrix for the other anodes are calculated in the same manner described in the previous steps. These calculated coefficients are used for the first guess of the scattering matrix. In order to conserve the photon count, the sum of each row of scattering matrix (representing one anode under observation and its contribution in all neighboring anodes of MAPMT) is normalized to 1.
(vi) The mean value observed in step (iv) is also considered as the first guess of emission photon scattering strength i.e.$\hat{\alpha}^{(1)}$.

We processed the simulated MMM image by initializing of the parameters as discussed above. The iteration process, as shown in Fig. 3, seeks to maximize the log-likelihood function and assigns the scattered emission photons of the ghost images to the original spatial locations. During the iterative process we defined two constraints; first total number of photons of the MMM images is constant before and after the processing, and second the positivity of the pixel values (as the fluorescence signal cannot be negative). The reconstruction process took around 10 iterations and Fig. 4(c) shows the processed image. It can be visually observed that all the ghost images are completely suppressed in the final reconstructed image. The bead intensity is increased after processing, representing the reassignment of photons from the ghost image locations. Quantified results for the improvement in signal strength and signal-to-ghost image ratio (SGR) are presented later in this paper.

Alphabets in a 2 by 2 MMM image. Next, we tested our reassignment method in a simulation of an alphabet image. The alphabet image contains certain shapes and overlaps that provide more complexity as compared to the simulated beads image. Again, an original image without ghost images was generated [Fig. 4(d)] as the reassignment target. Then, ghost images were imposed on all sub-images in the way that one sub-image in a 2 by 2 MMM image contains one primary alphabet image with the ghost images of the other three alphabets [Fig. 4(e)]. A given scattering-affected sub-image contains 100% of the intensity from a primary sub-image, 20% of the intensity from the two nearest neighbor sub-images along the horizontal and vertical directions, and 14% of the intensity of the farther neighbor along the diagonal direction. To start the iteration process the first guess of the scattering matrix and emission photon scattering strength was calculated as before. The final processed image, shown in Fig. 4(f) shows a cleanly reconstructed alphabet similar to the original. Clearly, the effects of ghost images are significantly suppressed from the MMM images by using the proposed approach. As discussed before, the image intensity of the processed image is higher than the original simulated image because of the reassignment of the ghost image photons to their original spatial locations from which they were scattered.

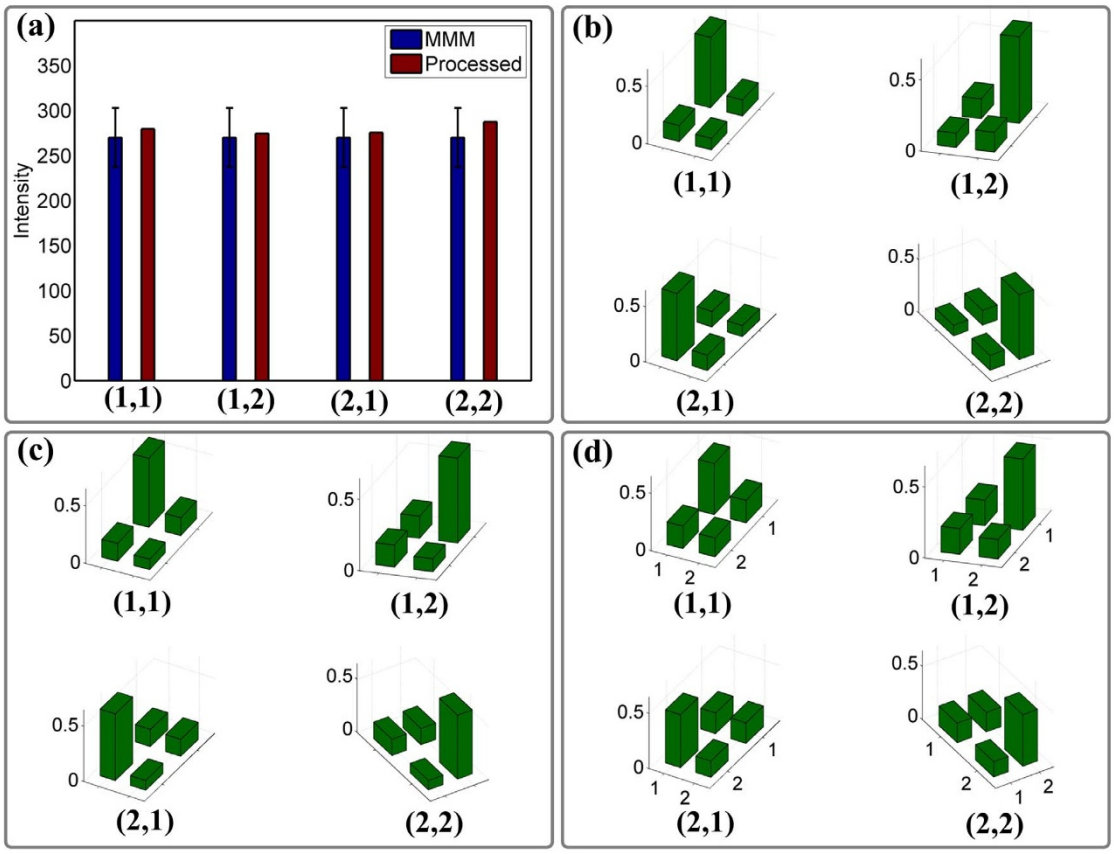

Figure 5 | (a) Intensity comparison of the simulated beads MMM image (blue, main anode + ghosts, subjected to Poisson noise) and their processed images (red) showing photon conservation after the process. (b–d) Scattering matrix elements distribution at 2 by 2 MMM anodes. (b) Original distribution used in simulation, (c) estimated distribution of the processed bead image, and (d) the alphabet image. One sub-image contains primary element of scattering matrix from the corresponding anode of image, and three scattering matrix elements showing the leakage of emission photons to the neighbor anodes due to scattering.

To evaluate the performance of the proposed method, we quantitatively analyzed the reconstruction results. Fig. 5(a) demonstrates photon conservation between the total intensity of the simulated MMM bead images and the processed images after photon-reassignment. The intensities of the simulated bead and its ghost images in the MMM image are summed and the sum is compared with the summed intensity of the same beads in the processed image. The error bars, in the MMM images, show the range of Poisson noise added in the simulation. Clearly, the reconstructed intensities at the different anode locations are within this Poisson noise range demonstrating that our algorithm conserves photons when signals from the ghost images are reassigned to correct spatial locations. Next, we compared elements of the scattering matrix corresponding to different anodes. The scattering matrix elements for the (1,1) anode should be [0.61 0.14 0.14 0.1] based on the preset parameters and the acquired emission photon scattering strength with normalization, and the same ratio follows for other anodes depending on their spatial locations. Our target is to compare the recovered scattering matrix elements based on the proposed approach with the original one used for simulation. Fig. 5(b) shows the original scattering matrix elements used for simulation of both bead and alphabet images. Fig. 5(c) and (d) show the reconstructed scattering matrix elements for the bead and alphabet images respectively. In both cases, the reconstructed scattering matrix matches very well the original values used to generate this simulation.

The accuracy of the proposed method is evaluated with known underlying structures and with realistic noise level. We demonstrate that the proposed algorithm can accurately recover the expected features, and that the photon number is conserved between the simulated and processed images as expected for correct reassignment. The first guess of unknown parameters can often be estimated with good accuracy, as discussed above, resulting in a faster, more accurate MLE process. In order to further demonstrate the influence of the first guess we processed the MMM alphabet image using different first guess estimates and quantitatively compared the results. Fig. 6(a) shows the reconstruction results (same number of iterations used to process Fig. 4(f)) when using an incorrect first guess. For the incorrect first guess, we used half the intensity ratios used for the correct initial guess. Fig. 6(b) shows the quantitative comparison of the processed results from the incorrect first guess to those obtained using the correct first guess. It can be clearly observed that in the case of wrong first guess the signal recovery is not complete and photons corresponding to ghost images remain at the neighboring anodes. The recovery of the correct reconstruction results, for the wrong initial guess, can be possible by increasing the number of iteration. We observed that for the wrong guess (used for the Fig. 6(a)), the correct reconstruction result is achieved when the number of iterations is doubled. Therefore the effect of incorrect first guess mainly results in added computation time but not at the expense of an incorrect image.

Experimental results. *Fluorescent beads image in 6 by 6 MMM with 85 μm foci separation*. We tested our proposed approach with a fluorescent bead image taken from the 6 by 6 MMM (with foci separation 85 μm). The sample was imaged in the 8 by 8 MMM system described in Sec. 2.1. The image was trimmed to contain only 6 by 6 sub-fields for further image processing due to low signal levels at the edge of the field of view. The sample was

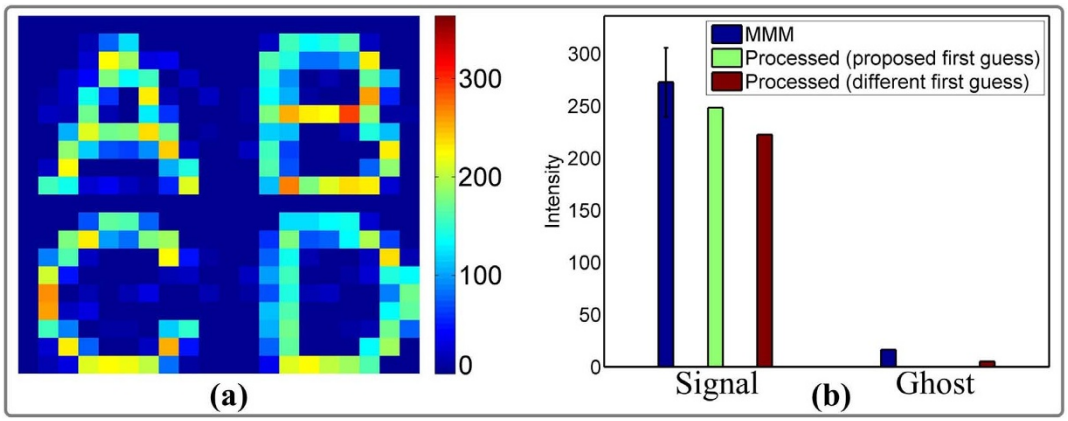

Figure 6 | **(a) Processed alphabet image when using different first guess (b) Signal and ghost image intensity comparison of the simulated MMM image (blue, main anode + ghosts, subjected to Poisson noise) and processed images at an anode with proposed first guess (green) and different first guess (red).**

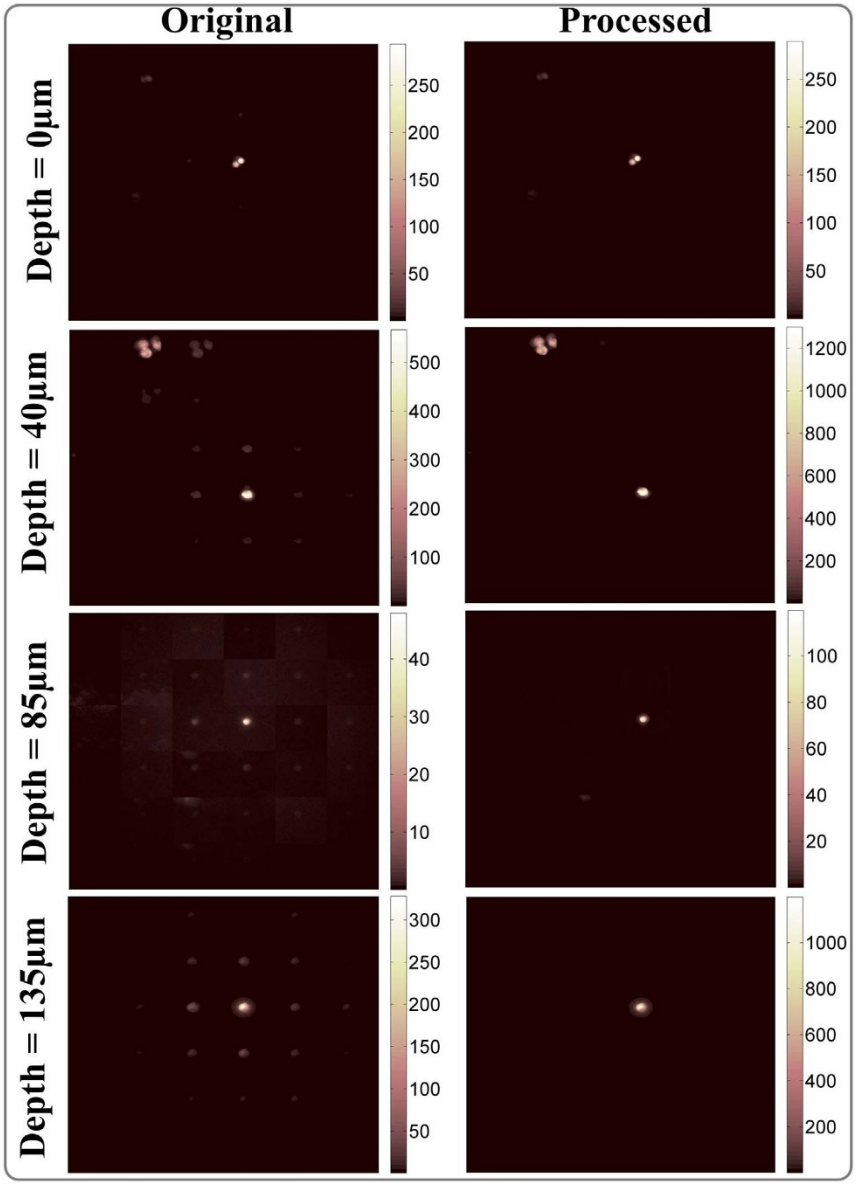

Figure 7 | **Left column: fluorescent beads images with the 6 by 6 MMM system at four imaging depths.** Right column: Corresponding processed images.

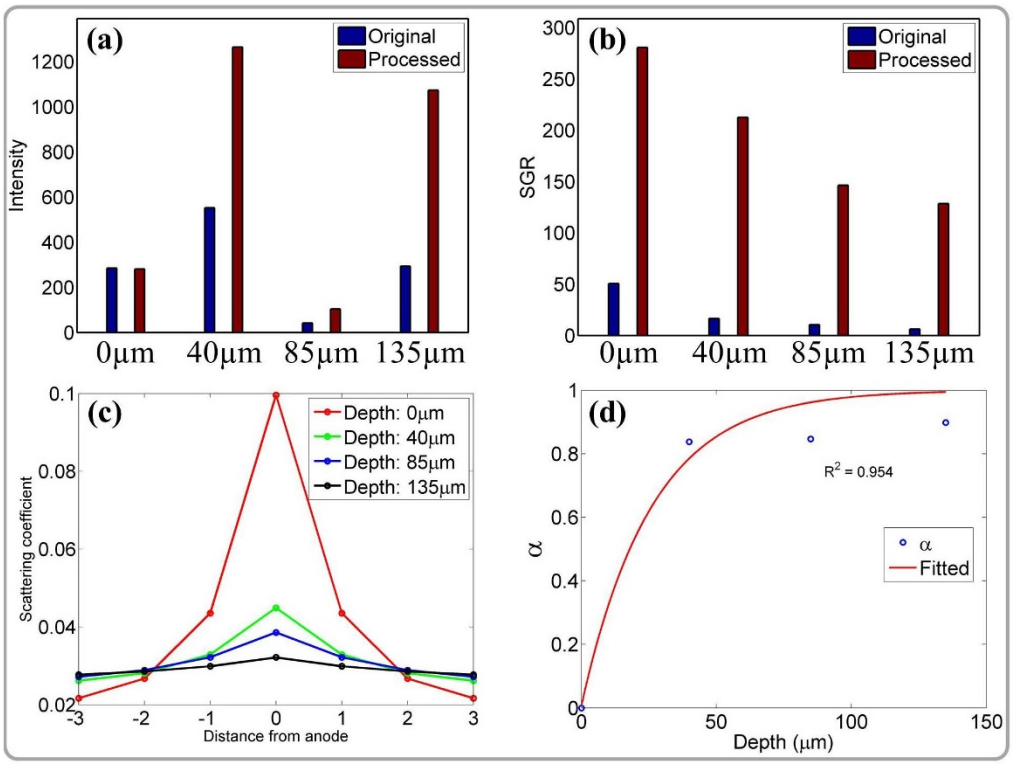

Figure 8 | (a) Bead's signal comparison at different depths for original and processed image. (b) Signal-to-Ghost ratio (SGR) of the imaging beads at different imaging depths, (c) Plot of scattering matrix elements for an anode and its distribution at neighboring anodes corresponding to different imaging depths of fluorescence beads image, (d) Plot of emission photon scattering strength as a function of imaging depth.

prepared with 10 and 15 µm diameter fluorescent latex microspheres (F8836 and F21010, Molecular Probes, Eugene, OR) immobilized in 3D by a 2% agarose gel. A 2% fat emulsion (Microlipid, Nestle, Vevey, Switzerland) was added to mimic the scattering characteristic of a tissue specimen.

The left column of Fig. 7 shows the acquired fluorescent beads MMM images at four different depths (0 µm, 40 µm, 85 µm, and 135 µm). As expected, the scattering effect intensifies with increased imaging depth resulting in more prominent ghost images. To suppress the effect of the ghost images and to reassign the photons of the ghost images to their original spatial locations, we used our proposed method. For the 6 by 6 MMM image, total $36 \times 36 = 1296$ coefficients are necessary for the scattering matrix C. As the scattering effect is different with depth, it is necessary to separately estimate the first guess of the scattering matrix and emission photon scattering strength for each depth. To start the photon reassignment iteration process, we used the same criteria described in section 3.1.1 to evaluate the first guess of the scattering matrix and scattering strength. The iteration process took around 30 iterations and the right column of Fig. 7 shows the processed images at their corresponding depths. Clearly, most of the strong ghost images were removed successfully, and only the primary bead images were left with better signal strength. To understand the performance of the proposed method on the signal levels of the imaging bead and its effect on the ghost image, we analyzed some of the relevant imaging parameters of the original and the processed MMM image.

Fig. 8(a) shows the strength of the signal of the bead at its original spatial location before and after processing. As expected, the strength of the signal is higher for the processed images, particularly at the larger imaging depths since the processing provides the reassignment of photons from the ghost image locations to the original bead location and thus increases the strength of the signal. This improvement in signal is expected to be higher for the larger imaging depths because the higher scattering contributes to stronger ghost images. To analyze the performance of the proposed method more precisely, the ratio of the signal at original bead location to the signal detected at its strongest ghost image location was calculated, and termed signal-to-ghost ratio (SGR), as shown in Fig. 8(b). SGR was calculated for original and the processed images at each imaging depth. As expected, the SGR is highest for the shallowest imaging depth because of low scattering. The SGR of the original image, which is significantly lower for the large imaging depth because of severe scattering, is substantially recovered in the processed image. The increase of the SGR at 0 µm depth even with no intensity change is due to the suppression of the background noise during processing.

Elements of scattering matrix at the bead image location anode and adjacent nearest neighbors were analyzed for different imaging depth, as shown in Fig. 8(c). As the imaging depth increases, due to increase in the emission scattering the scattering matrix elements become flatter so that the ratio of main anode to neighboring anodes decreases as previously investigated in Ref [25]. This effect is further elaborated by plotting the values of emission photon scattering strength acquired at different imaging depths, as shown in Fig. 8(d). As the imaging depth increases, the emission photon scattering strength increases exponentially as expected.

Mouse brain imaging in 4 by 4 MMM with 85 µm foci separation. We next tested our approach with a mouse brain image taken in the 4 by 4 MMM system. Thy1-GFP transgenic mice[26] had surgery for cranial windows that were bilaterally implanted over the visual cortices between 6–8 weeks of age[27]. These mice express green fluorescent protein (GFP) in a sparse pseudo-random subset of neocortical neurons. Imaging was performed on adult mice (>3 months) previously implanted with cranial windows. Mice were anesthetized with isoflurane (3% for induction and 1.5% during imaging). Anesthesia was monitored by breathing rate and foot pinch reflex. The head was positioned in a custom made stereotaxic restraint affixed to a stage. Cell body and dendritic arbors of inhibitory neurons labeled with

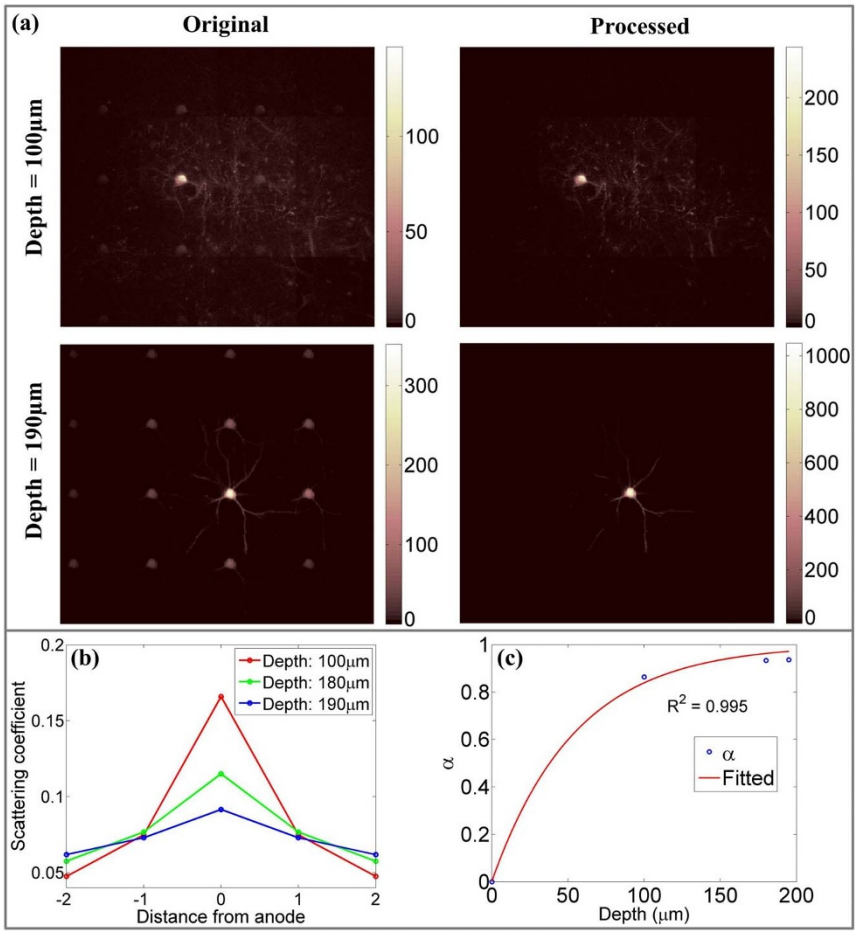

Figure 9 | **(a) A mouse brain image with the 4 by 4 MMM system. Left acquired images at 100 μm and 190 μm imaging depths, and Right are the corresponding processed images, (b) Plot of scattering matrix elements for an anode and its distribution at neighboring anodes corresponding to different imaging depths of mouse brain, (c) Plot of emission photon scattering strength as a function of imaging depth.**

GFP in layers 2/3 of visual cortex were imaged. The excitation wavelength was 910 nm, the laser power per focus was about 42 mW, the dwell time was 40 μs with 0.5 μm pixel, and the image size was 340 μm × 340 μm with 4 × 4 foci.

The left column of Fig. 9(a) shows the MMM images of the mouse brain at 100 μm and 190 μm imaging depths. Ghost images can be visually observed at both depths; they are, of course, more prominent for the larger imaging depth. The proposed approach was used to suppress the effect of the ghost images and to reassign the photons of the ghost images to their original spatial locations. For the 4 by 4 MMM image, total 16 × 16 = 256 coefficients are necessary for the scattering matrix C. We used the same criteria as described above to evaluate the first guess of the scattering matrix and emission photon scattering strength. Processed images are shown in Fig. 9(a), the right column at the corresponding depths. The accuracy of the approach can be seen in the removal of all ghost cell bodies. Further, the resultant final images contain realistic dendrite branches that are connected to the neuron body, and without unconnected branches, as would be expected from known neuronal anatomy. We chose this sparse image to test the recovery of real image features after reassignment because we can easily trace the neuronal dendrite. With the expectation of similar behavior of imaging parameters as shown in Fig. 8, we analyzed the behavior of scattering matrix elements and scattering strength at different depths and Fig. 9(b) and (c) show the plot of their values as a function of depth. Similar to the result of the bead sample in section 3.2.1, the scattering matrix becomes flatter as the imaging depth increases showing more widely spread emission photons due to scattering. As expected, the emission photon scattering strength fits well to an exponential function.

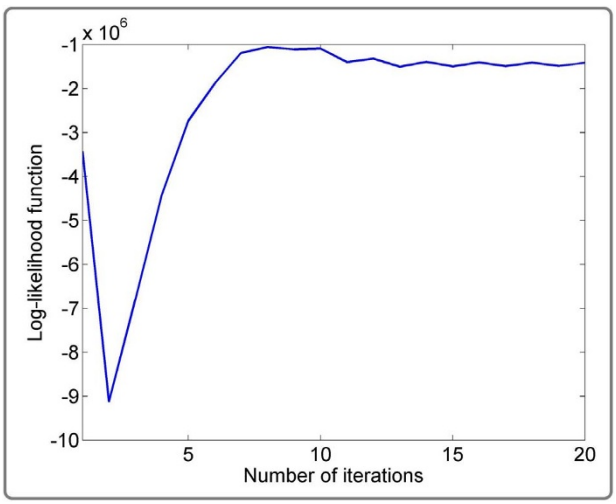

Figure 10 | **Plot of log-likelihood function for number of iterations.**

Fig. 10 shows the plot of log-likelihood function versus number of iterations for the processing of mouse brain images as shown in Fig. 9(a). Convergence of the log-likelihood function starts at around 15 iterations, which provides the final processed image. It should be noted that imaging time and image processing time are not equivalent, especially for *in vivo* experiments. For example, the increase in

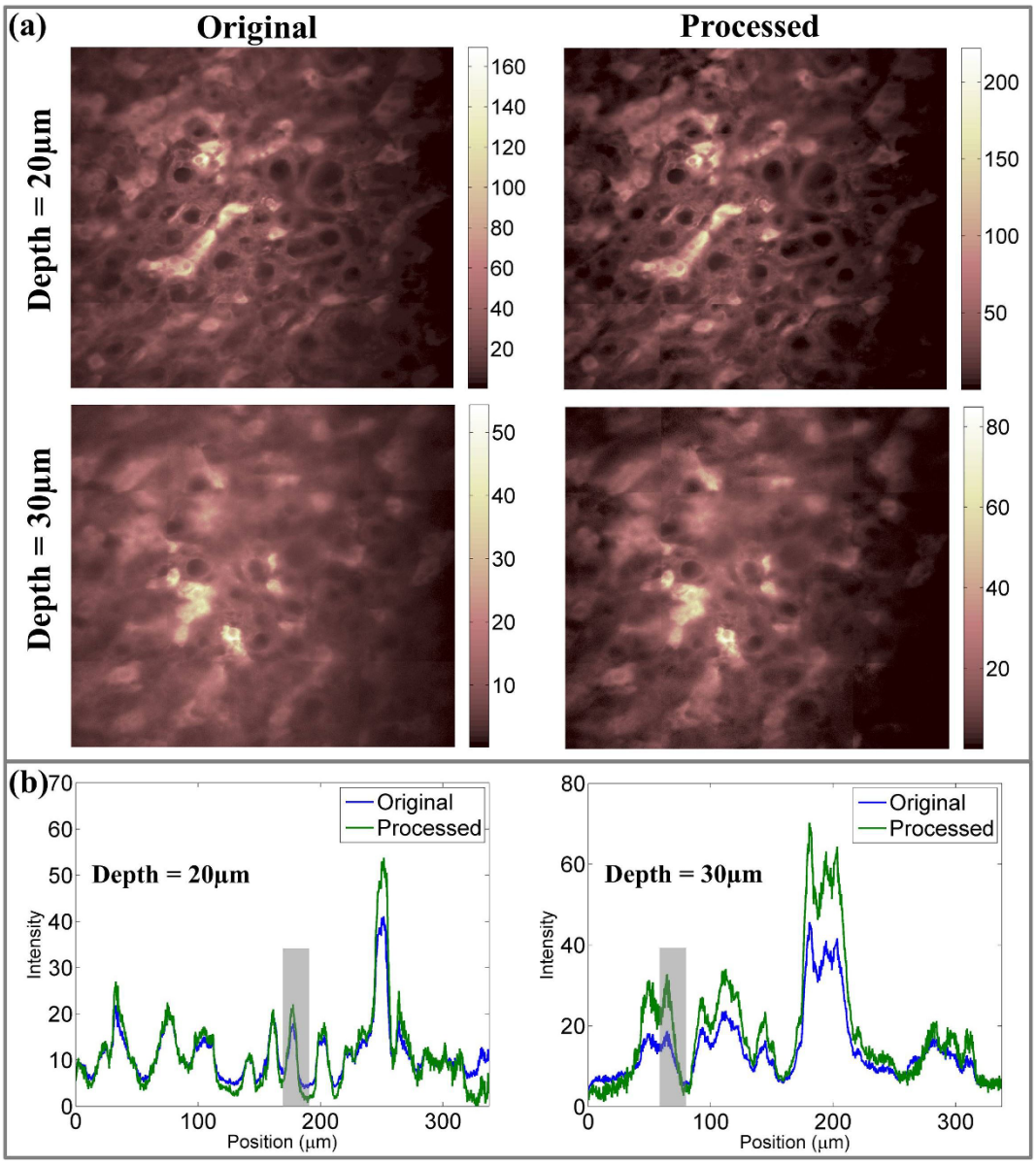

Figure 11 | Liver image with the 6 by 6 MMM system. (a) Left acquired images at 20 µm and 30 µm imaging depths, and right are the corresponding processed images. (b) Intensity line plots for original and processed images for imaging depths 20 µm and 30 µm respectively.

imaging speed using MMM reduces the typical time, from approx. 90 minutes (pixel residence time: 40 µs, 756 × 756 pixels scanned per XY plane using single focus excitation, 125 XY planes in Z stack) to approx. 6 minutes (16 pixels at the same residence time of 40 µs), for high resolution imaging of an entire neuronal volume in the brain of a living mouse. This reduction in image acquisition time is critical in terms of reducing anesthetic duration to minimize physiological influence and animal attrition. Further, we observed that with equal pixel residence time, the 4 by 4 MMM imaging system improves imaging speed by 16 fold compared to a typical single focus multi-photon excitation fluorescence microscope, but maintains almost equivalent image SNR. The total computational time taken for processing two 4 by 4 MMM images was around 40 seconds using a standard desktop computer with i5 processor. This is about 10 times longer than the time for image acquisition but still substantially shorter than single focus acquisition. More importantly, the processing time could easily be reduced to below image acquisition speed by parallelizing computation with graphical processing units (GPUs). With ever increasing and cheap computation power, we have no doubt that the bottleneck lies in physical image acquisition rather than image processing.

Table 1 | Contrast comparison of original and processed liver images for imaging depths 20 µm and 30 µm

	Original	Processed
Depth: 20 µm	0.62	0.87
Depth: 30 µm	0.54	0.81

Liver tissue imaging using 6 by 6 MMM with 85 µm foci separation. We further tested our approach with liver tissue imaging containing significantly denser features. The imaging was performed with a 6 by 6 MMM system with 85 µm foci separation. The livers of male Wistar rats with an average weight of 200 g that underwent bile duct ligation surgeries were harvested in accordance to the Institutional Animal Care and Use Committee regulations at the Biological

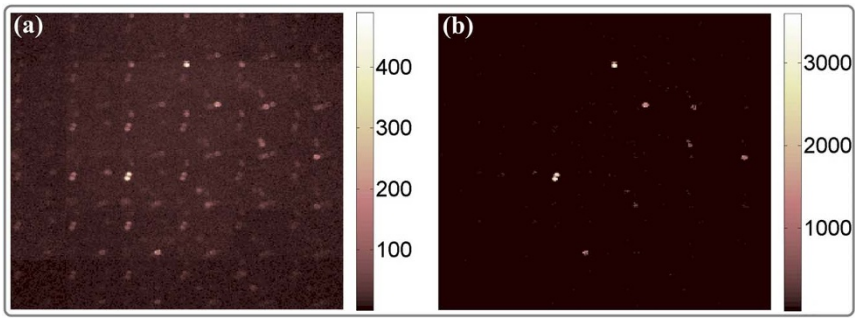

Figure 12 | (a) MMM Fluorescent beads image with the 6 by 6 MMM system (with 45 μm foci separation), and (b) is the corresponding processed image.

Resource Center of A*STAR Singapore[28]. The liver tissue specimens were obtained from the paraffin preservation of the livers after fixation by cardiac perfusion with 4% paraformaldehyde.

Fig. 11(a) shows the original MMM image and the processed image of the liver tissue sample at 20 μm and 30 μm imaging depths. The ghost images in MMM are not so prominent. Because of the dense features scattering mainly generates a relatively uniform background haze at the neighboring anodes. In this case, the proposed method suppresses the photons in the uniform background haze and reassigns them to the original anode location. Fig. 11(b) shows the intensity line plots for both imaging depths. It can be clearly observed that for the processed images the background noise is suppressed and image features are extracted with better signal strength. Contrast of the features, highlighted in Fig. 11(b) at the 20 μm and 30 μm imaging depths, is calculated for the original and processed image. The quantitative comparison of contrast is shown in Table 1. Clearly, the proposed method improves feature contrast; essentially because of the improvement in signal strength due to concurrent suppression of the background haze at the respective anode and more effective utilization of the available image photons.

Fluorescent beads and Mouse brain imaging in MMM with 45 μm foci separation. We tested our proposed approach with a fluorescent beads taken from MMM system with 45 μm foci separation. The reduced separation of the foci, for the same scattering conditions increases the crosstalk between foci and results in stronger ghost images. The bead sample was prepared with 4 μm diameter fluorescent latex microspheres (F8858, Molecular Probes, Eugene, OR) immobilized in 3D by 2% agarose gel. A 2% intralipid emulsion (Liposyn III, Abbott Laboratories, North Chicago, IL) was added to mimic the scattering characteristic of a tissue specimen.

Fig. 12(a) shows the raw fluorescence bead image taken from the 8 by 8 MMM with foci separation of 45 μm at images at a depth of 150 μm. This image was trimmed to contain 6 by 6 sub-fields for further image processing. Fig. 12(b) shows the processed image after photon reassignment. As expected, due to the smaller foci separation emission photons were scattered more into the adjacent neighboring anodes of the MAPMT resulting in more pronounced ghost images. We used our proposed approach to suppress the ghost images in such a severe scattering case. From the processed image shown in Fig. 12(b), we can visually observe that the ghost images are significantly suppressed, and the remaining dim signal represents beads situated in neighboring axial planes. Despite the same sample scattering due to the smaller foci separation, emission photon scattering strengths were 0.98 for 45 μm foci separation at 150 μm imaging depth as compared to 0.88 for 85 μm foci separation at 135 μm imaging depth.

Mouse brain imaging in MMM with 45 μm foci separation. Finally, we tested our approach for a mouse brain image taken from the MMM system with 45 μm foci separation. For the mouse brain imaging, a Thy1-GFP transgenic mouse[26] was deeply anesthetized with 2.5% Avertin (0.025 ml/g i.p.) and transcardially perfused with PBS, followed by 4% paraformaldehyde. Its brain was dissected and placed overnight in cold 4% paraformaldehyde. 300 μm thick coronal sections were sectioned with a vibrotome, then mounted and coverslipped on microscope slides using adhesive silicone isolators (JTR20-A2-1.0, Grace Bio-Labs, Bend, OR).

Fig. 13(a) shows the mouse brain image taken at 90 μm imaging depth using the 8 by 8 MMM system with 45 μm foci separation. This image was trimmed to contain 6 by 6 sub-fields for further image processing. It can be observed that the ghost images from neighboring foci are substantial and these ghost images are intricately mixed with the "real" image features. Furthermore, a uniform background haze due the dense features of sample, as discussed before, can also be clearly visualized. We processed the image by using the same convergence criteria and the same method for estimating the first guess of the scattering matrix and scattering strength parameters. The processed image is shown in Fig. 13(b). Apparently, the ghost images and background haze are simultaneously suppressed from the processed image while the photons are assigned back to the real image. Thus it provides better contrast and SGR. Fig. 13(c) and (d) show the intensity line plots in the x- and y-directions, along the dotted lines shown on Fig. 13(a). Improvement of the signal and suppression of the ghost images can be clearly observed from the intensity line plots. One particular region highlighted in the images shows the overlap of ghost image with true image features. The recovery of the image features while simultaneously suppressing the ghost image can be observed in the processed image. We further show other imaging parameters e.g. strength of the neuronal signal at its original spatial location before and after processing (Fig. 13(e)), and distribution of the neuronal scattering matrix at the correct image anode location and as a function of the distance from this location (Fig. 13(f)).

Conclusions

MMM has the advantage of improved imaging speed critical for *in vivo* imaging applications. However, due to scattering in turbid specimens MMM images suffer from ghost images especially at higher imaging depths. Previously, these ghost images have been processed using the scattering coefficients acquired experimentally. However, the experimental estimation requires frequent measurement with different specimens, different locations, and at different imaging depths. In this paper, we propose estimating the scattering coefficients for the photon reassignment process based on the maximum likelihood (ML) estimation. This image post-processing method increases the SNR and SGR of the final processed image by reassigning the scattered photons to the original spatial locations, and also avoids experimental calibration of the scattering matrix resulting in greater experimental efficiency. It is also important to note that most experimental methods for calibrating the scattering matrix can only be performed on tissue phantoms or at a few locations in the specimen, so that inevitable errors in matrix estimation in other loca-

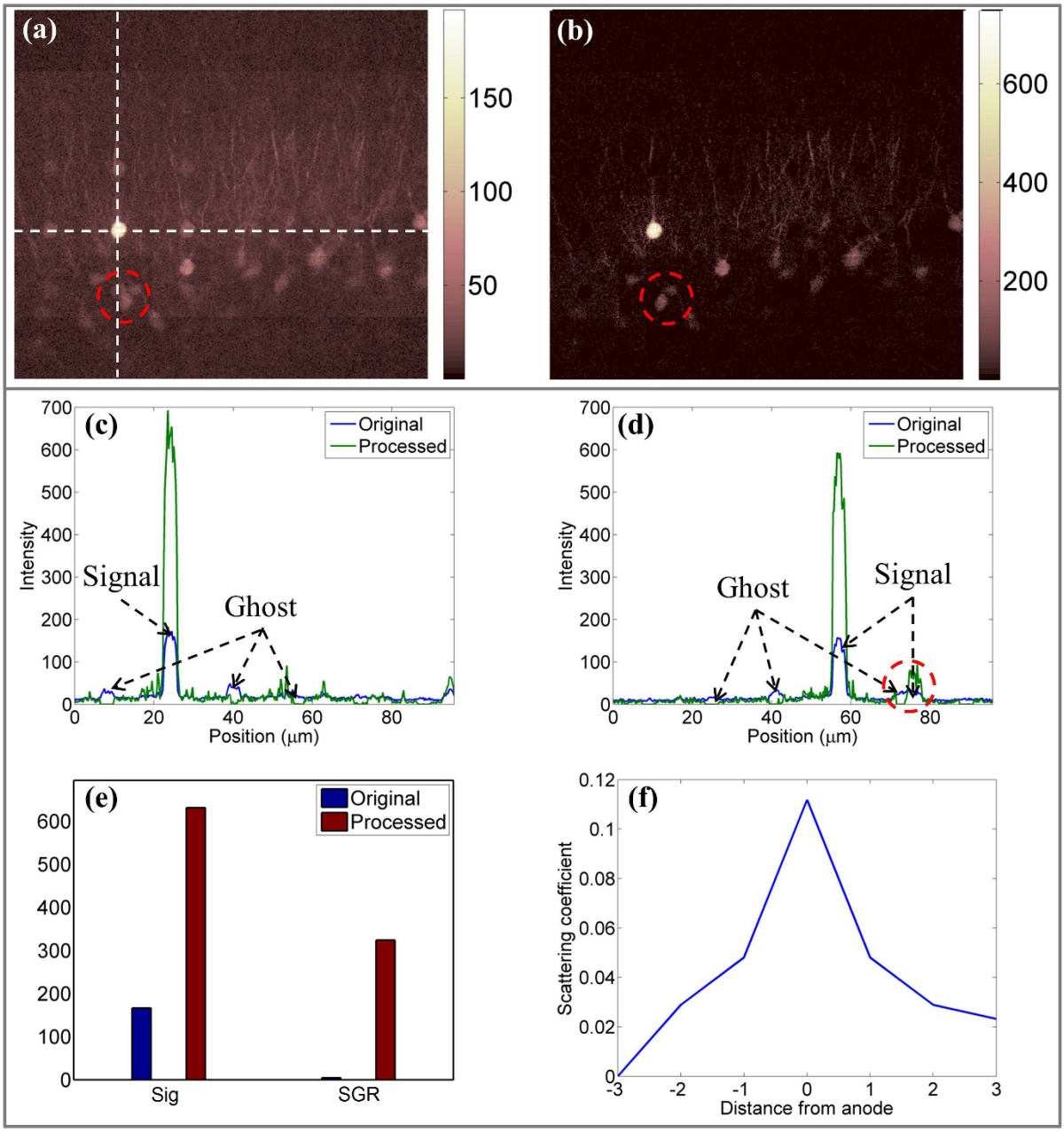

Figure 13 | (a) Image of GFP expressing neurons in a mouse brain acquired using a 6 by 6 MMM system at 90 μm depth, and (b) is the corresponding processed image. (c) and (d) Intensity line plots in x- and y- directions for the mouse brain image, (e) Signal and SGR comparison for original and corresponding processed image, and (f) plot of the scattering matrix elements for an anode and its distribution at neighboring anodes.

tions will greatly degrade reassignment accuracy and introduce systematic error. This problem is completely avoided using our new approach where the only a priori parameters used are the physical properties of the optical system such as the objective numerical aperture and the light wavelengths. We have shown the feasibility of our approach with simulated results and confirmed that the algorithm can estimate the scattering coefficients and reassign ghost images to their correct location. We validated our approach with fluorescent bead samples in the turbid medium, as well as with *in vivo* mouse brain images. The processed images demonstrate that the scattered emission photons are reassigned to their original spatial locations resulting in higher signal. The SGR is improved by up to a factor of 10. The algorithm also confirms that shorter foci separation generates more crosstalk, and the emission photon scattering strength increases as a function of imaging depth. To minimize the crosstalk between foci and the resulting ghost images inherently, it is recommended to adopt a large field of view objective lens and maximize foci separation. However, in the case that only small field of view objective lenses are available or the region of interest is small, our proposed approach can be a good solution for image post processing and image recovery. It is also interesting that our approach can recover the scattering matrix and the emission photon scattering strength at each image location allowing us to quantitative recover tissue optical properties locally.

1. Denk, W., Strickler, J. H. & Webb, W. W. 2-PHOTON LASER SCANNING FLUORESCENCE MICROSCOPY. *Science* **248**, 73–76 (1990).
2. So, P. T. C. *et al.* Two-photon excitation fluorescence microscopy. *Annu. Rev. Biomed. Eng.* **2**, 399–429 (2000).

3. Svoboda, K. *et al.* In vivo dendritic calcium dynamics in neocortical pyramidal neurons. *Nature* **385**, 161–165 (1997).
4. Ragan, T. *et al.* Two-photon tissue cytometry. *Methods Cell Biol.* **75**, 23–39 (2004).
5. Kim, K. H. *et al.* Three-dimensional tissue cytometer based on high-speed multiphoton microscopy. *Cytometry A* **71**, 991–1002 (2007).
6. Chen, J. L. *et al.* Clusteres Dynamics of Inhibitory Synapses and Dendritic Spines in the Adult Neocortex. *Neuron* **74**, 361: 373 (2012).
7. Kim, K. H., Buehler, C. & So, P. T. C. High-speed, two-photon scanning microscope. *Appl. Opt.* **38**, 6004–6009 (1999).
8. Fan, G. *et al.* Video-rate scanning two-photon excitation fluorescence microscopy and ratio imaging with cameleons. *Biophys. J.* **76**, 2412–2420 (1999).
9. Iyer, V., Losavio, B. E. & Saggau, P. Compensation of spatial and temporal dispersion for acousto-optic multiphoton laser-scanning microscopy. *J. Biomed. Opt.* **8**, 460 (2003).
10. Reddy, G. D. & Saggau, P. Fast three-dimensional laser scanning scheme using acousto-optic deflectors. *J. Biomed. Opt.* **10**, 064038 (2005).
11. Zeng, S. *et al.* Simultaneous compensation for spatial and temporal dispersion of acousto-optical deflectors for two-dimensional scanning with a single prism. *Opt. Lett.* **31**, 1091–1093 (2006).
12. Katona, G. *et al.* Fast two-photon in vivo imaging with three-dimensional random-access scanning in large tissue volumes. *Nat. Methods* **9**, 201–208 (2012).
13. Cianci, G. C., Wu, J. & Berland, K. M. Saturation modified point spread functions in two-photon microscopy. *Microsc. Res. Tech.* **64**, 135–141 (2004).
14. Zipfel, W. R., Williams, R. M. & Webb, W. W. Nonlinear magic: multiphoton microscopy in the biosciences. *Nat. Biotechnol.* **21**, 1369–1377 (2003).
15. Oron, D., Tal, E. & Silberberg, Y. Scanningless depth-resolved microscopy. *Opt. Express* **13**, 1468–1476 (2005).
16. Zhu, G. *et al.* Simultaneous spatial and temporal focusing of femtosecond pulses. *Opt. Express* **13**, 2153–2159 (2005).
17. Bewersdorf, J., Pick, R. & Hell, S. W. Multifocal multiphoton microscopy. *Opt. Lett.* **23**, 655–657 (1998).
18. Buist, A. H. *et al.* Real time two-photon absorption microscopy using multi point excitation. *J. Microsc. (Oxf.)* **192**, 217–226 (1998).
19. Nielsen, T. *et al.* High efficiency beam splitter for multifocal multiphoton microscopy. *J. Microsc. (Oxf.)* **201**, 368–376 (2001).
20. Kurtz, R. *et al.* Application of multiline two-photon microscopy to functional in vivo imaging. *J. Neurosci. Meth.* **151**, 276–286 (2006).
21. Jureller, J. E., Kim, H. Y. & Scherer, N. F. Stochastic scanning multiphoton multifocal microscopy. *Opt. Express* **14**, 3406–3414 (2006).
22. Amir, W. *et al.* Simultaneous imaging of multiple focal planes using a two-photon scanning microscope. *Opt. Lett.* **32**, 1731–1733 (2007).
23. Sacconi, L. *et al.* Multiphoton multifocal microscopy exploiting a diffractive optical element. *Opt. Lett.* **28**, 1918–1920 (2003).
24. Watson, B. O., Nikolenko, V. & Yuste, R. Two-photon imaging with diffractive optical elements. *Front. Neural Circuits* **3** (2009).
25. Kim, K. H. *et al.* Multifocal multiphoton microscopy based on multianode photomultiplier tubes. *Opt. Express* **15**, 11658–11678 (2007).
26. Feng, G. *et al.* Imaging neuronal subsets in transgenic mice expressing multiple spectral variants of GFP. *Neuron* **28**, 41–51 (2000).
27. Lee, W. C. A. *et al.* A dynamic zone defines interneuron remodeling in the adult neocortex. *Proc. Natl. Acad. Sci. USA* **105**, 19968–19973 (2008).
28. He, Y. *et al.* Towards Surface Quantification of Liver Fibrosis Progression. *J. of Biomed. Opt.* **15**, 056007 (2010).

Acknowledgments

This research was supported by grant RO1 EY017656, National Research Foundation Singapore through the Singapore MIT Alliance for Research and Technology's BioSystems and Micromechanics Inter-Disciplinary Research programme, NIH P41EB015871, 5 R01 NS051320, 4R44EB012415, NSF CBET-0939511, the Singapore-MIT Alliance 2, the MIT SkolTech initiative, the Hamamatsu Corp., Engineering Research Center (2011-0030075) of the National Research Foundation (NRF) funded by the Korean government and the Koch Institute for Integrative Cancer Research Bridge Project Initiative.

Author contributions

P.T.C.S., E.N. and H.Y. designed the project. J.W.C. and V.R.S. wrote the manuscript text and prepared the figures. J.W.C., K.H.K. and P.T.C.S. designed the experimental system and acquired the image data. V.R.S. and P.T.C.S. prepared the algorithm and processed the data. J.S., Q.P. and E.N. prepared the biological samples and wrote the respective sections of the manuscript. E.N., P.T.C.S. and H.Y. analyzed the results and contents of the manuscript. All authors participated in the discussion and commented on the manuscript.

Additional information

Competing financial interests: The authors declare no competing financial interests.

How to cite this article: Cha, J.W. *et al.* Reassignment of Scattered Emission Photons in Multifocal Multiphoton Microscopy. *Sci. Rep.* **4**, 5153; DOI:10.1038/srep05153 (2014).